*energies*

MDPI

*Article*

# Design and Performance Study of Large-Angle Inlet Guide Vane with Contraction Channels

**Qingyi Sai *, Bo Qin, Jin Zhao and Lingshu Meng**

College of Energy and Power Engineering, University of Shanghai for Science and Technology, Shanghai 200093, China; 222210066@st.usst.edu.cn (B.Q.); 222210100@st.usst.edu.cn (J.Z.); mls3391a@gmail.com (L.M.)
* Correspondence: saiqingyi@163.com

**Abstract:** Negative inlet pre-swirl has been identified as a potentially effective method to improve the theoretical work that has been performed. However, it should be noted that a large negative inlet swirl may adversely affect the pressure ratio of the compressor due to the different centrifugal forces generated by the movement of the airflow within the large-angle pre-swirl guide vane flow channel. In order to achieve a large inlet negative pre-swirl, a new guide vane with a contraction channel is proposed for a 40° pre-swirl angle fan. This contraction guide vane is of the tandem type, and it includes a first-stage enlarged guide vane and a second-stage contraction guide vane channel. Comprehensive CFD numerical simulations and experimental studies have been conducted to analyze the key design parameters, and the total pressure loss and efficiency of the new guide vanes were analyzed and compared under various operating conditions. It was found that this new guide vane can significantly reduce the total pressure loss coefficients. Compared with the conventional guide vanes, the inlet velocity distribution is more uniform development of inlet velocities, and a significant reduction in flow separation is found for this new guide vane. The guide vane with a ring width ratio of 1.5 reduced 53.11% of the total pressure loss coefficient. In addition, the efficiency of the fan has been shown to increase by more than 2.29% under various operating conditions, due to the improved internal flow of the fan under large flow conditions, under all operating conditions, with an overall improvement in the total pressure ratio of about 5%.

**Keywords:** large pre-swirl angle; inlet guide vane; contraction channel; total pressure loss; high efficiency; pressure ratio

check for updates

Received: 28 January 2025
Revised: 16 February 2025
Accepted: 22 February 2025
Published: 24 February 2025

**Citation:** Sai, Q.; Qin, B.; Zhao, J.; Meng, L. Design and Performance Study of Large-Angle Inlet Guide Vane with Contraction Channels. *Energies* **2025**, *18*, 1085. https://doi.org/10.3390/en18051085

**Copyright:** © 2025 by the authors. Licensee MDPI, Basel, Switzerland. This article is an open access article distributed under the terms and conditions of the Creative Commons Attribution (CC BY) license (https://creativecommons.org/licenses/by/4.0/).

## 1. Introduction

The research on the theoretical energy of turbomachinery is of great significance in engineering applications [1–3]. The improvement in the theoretical energy is helpful to improve the energy conversion efficiency of turbomachinery. This is crucial for various types of energy conversion equipment.

Negative inlet pre-swirl contributes to enhancing the performance and efficiency of the equipment, as well as its adaptability under various operating conditions, which is usually realized by adjusting the inlet guide vane (IGV). Existing studies [4–6] have shown that the inlet pre-swirl formed by increasing the IGVs can effectively increase the operating pressure of compressors and fans.

Scientists have studied the inlet pre-swirl structure of the inlet with guide vanes [7–9] and found that the size of the guide vane cyclonic angle has the most significant effect on improving the theoretical power consumption [10–12]. Song Zishuai [13] studied the

influence of different guide vane inlet angles on the aerodynamic performance of the impeller. The results show that when the negative pre-swirl is performed, the total pressure ratio of the impeller increases first and then decreases with the change in the pre-swirl angle. When the pre-swirl angle exceeds 30°, the total pressure ratio of the impeller begins to decrease. HUANG Le [14] analyzed the effect of pre-swirl on compressor performance, and he found that the flow loss caused by the inlet swirl negatively affects the pressure ratio of the compressor, which is mainly due to the large centrifugal force generated by the gas as it undergoes pre-swirl flow. When the intensity of flow loss increases to a certain degree, especially when encountering an airflow deflection angle of more than 30°, it will make the compressor capacity decrease and produce obvious additional efficiency loss [15–17]. Okishi [18] conducted an experimental design and study on the straight-blade-type variable curvature guide vane, and the results of the study showed that the cascade aerodynamic loss increases rapidly after the deflection angle of the guide vane is more than 35°. Nguyen DucAnh [19] thoroughly investigated the effect of changing the inlet guide vane placement angle on the flow loss and proposed that 30° is the critical installation angle of the inlet guide vane, and when the deflection angle of the guide vane is too large, airflow separation on the suction side of the leading edge will be stronger, which restricts the range of the use of the inlet guide vane.

Currently, the research direction of most scholars still focuses on reducing the pressure loss caused by an excessive pre-swirl angle by improving the airfoil shape and structure of the guide vane. For example, NAJJAR [20] produced pre-swirl or even parabolic pre-swirl with a linear change along the blade height by twisting the IGV blade, and the feasibility of improving the pre-swirl performance by setting is proved by theory. Zheng Y [21] changed the profile of the blade cross-section from a single straight segment to two straight segments, increasing the blade chord length at the inner radius of the IGV has been demonstrated to effectively reduce the drag coefficient and increase the pre-swirl coefficient compared to the original blade. Steinke and Crouse [22] proposed a variable IGV and pointed out that the variable camber guide vane avoids the deterioration of the intake conditions after the rotation of the adjustable guide vane. Since then, a large number of studies have proved the advantages of variable camber guide vanes in practical applications [23–25]. Although the anti-separation ability of variable camber guide vanes is very strong, the low loss deflection angle can reach more than 32° [26].

In order to solve the problem of poor gas mobility due to centrifugal force during large-angle pre-swirl flow and to prevent it from affecting the downstream inlet backstage rotor vanes and the overall efficiency of the system, this paper adopts a tandem-type blade and a contracted channel structure and designs a kind of inlet of low-speed flow and then slowly accelerated by the leading vane, which is used to reduce the flow in the process of folding and turning. The centrifugal force generated during the movement makes the airflow in the channel stable and uniform folding, so as to realize the large-angle pre-swirl.

## 2. Pre-Swirl IGV Program Design

### *2.1. Principle and Structure of Pre-Rotating Inlet Guide Vane*

The speed triangle of the fan with inlet negative pre-swirl guide vanes is shown in Figure 1. When the gas is negative pre-swirl, $c_{1u} < 0$ increases the theoretical energy pressure head according to Euler's Equation (1), where $c_1$ is the absolute velocity of the leading vane outlet and the moving vane inlet; $c_2$ is the absolute velocity at the outlet of the moving vane; $u_1$ and $u_2$ are the circumferential velocities.

$$h_t = \frac{1}{g}(c_{2u}u_2 - c_{1u}u_1) \quad (1)$$

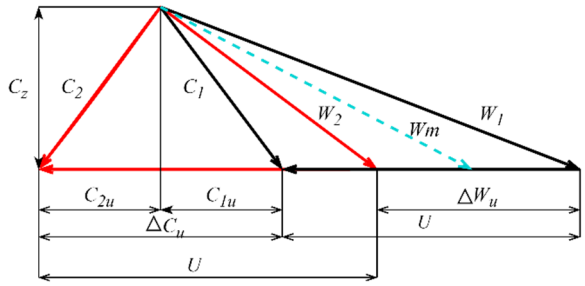
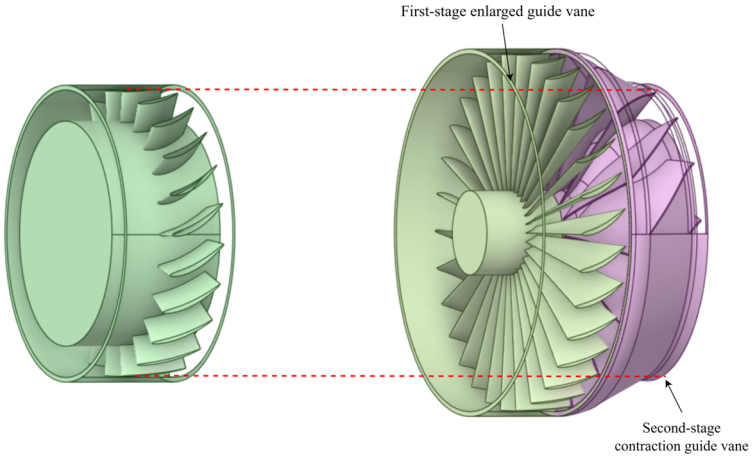



**Figure 1.** Negative pre-swirl high-pressure axial flow fan and velocity triangle diagram.

The conventional IGV channel is a single-stage, straight-cylinder channel, as illustrated in Figure 2a. The inlet and outlet diameters are equal, resulting in a consistent area on both sides. However, the velocity distribution becomes non-uniform as the gas traverses the guide vane due to the high airflow velocity at the inlet, particularly under conditions of high flow rate, which leads to the formation of separated flow.




(**a**) conventional IGV (**b**) contraction IGV

**Figure 2.** Structure of the contraction IGV and traditional IGV.

To reduce the centrifugal force generated by the movement of airflow in the folding process, a two-stage gradual contractile guide vane has been proposed and designed in this paper, named contraction IGV; this comprises a first-stage enlarged guide vane and a second-stage contraction guide vane, as illustrated in Figure 2b. Expanding the inlet area of the first-stage guide vane allows the airflow to enter the guide vane at a lower speed, and after passing through the first-stage guide vane, the airflow generates a certain degree of negative pre-swirl. Upon entering the second-stage contraction guide vane, the airflow experiences an acceleration, maintaining the gas in a state of original negative pre-swirl. The acceleration of the gas is found to be a gradual process, which consequently results in a reduction in the centrifugal force that is generated during the process of turning.

### *2.2. New Guide Vane Models*

An IGV of the high-pressure axial fan is used as a prototype [27], named P0, and the design aerodynamic parameters of the IGV of the fan are as follows: the design flow rate is 230 $m^3/h$, the inlet velocity of the airflow is 14.39 m/s, and the angle of the airflow into the moving vane after the gas passes through the guide vane is 40°. The airflow angle is 40°.

The total inlet area of the first-stage enlarged guide vane is determined by the axial velocity $c_z$; since the guide vane is designed to accelerate the gas slowly, three lower inlet velocities—4 m/s, 5 m/s, and 6 m/s—are selected for the study. The inlet annular surface

of the second-stage contraction channel guide vane is divided into three circulating annular surfaces. The width of the outer annular surface is designated as $h_1$, the width of the inner annular surface as $h_2$, in which the intermediate annular width $h_m$ is kept unchanged, and the ratio of the inner and outer annular widths is defined as ring width ratios $\xi = h_1/h_2$. As shown in Figure 3, the size of the ring width ratio $\xi$ affects the internal structure of the guide vane, altering the acceleration process of airflow in the second-stage constriction channel. Therefore, to find the optimal ring width ratio $\xi$, in this paper, on the basis of ensuring that the inlet velocity remains constant, different ring width ratios $\xi$ are selected to adjust the size of the outer ring surface width and the inner ring surface width, so as to optimize the internal structure of the guide vane. To study the differences in the acceleration characteristics of airflow passing through the second-stage constriction channel under a different ring width ratio $\xi$. Based on the selection of three different airflow inlet velocities, three sets of contraction IGV with varied configurations were designed in this paper, and specific parameters are shown in Table 1.

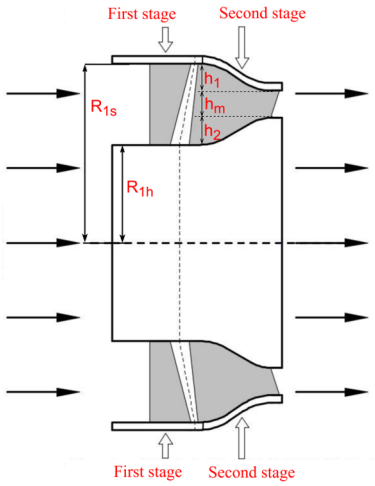



**Figure 3.** Dimensions of contraction IGV structure.

**Table 1.** Dimensional parameters of meridian runner structure for each scheme of IGV.

| Case | cz/m/s | h1/mm | h2/mm | ξ = h1/h2 | R1s |
|---|---|---|---|---|---|
| A1 | 4 | 14.82 | 29.64 | 0.5 | 75.32 |
| A2 | 4 | 18.28 | 18.28 | 1.0 | 78.78 |
| A3 | 4 | 21.38 | 10.69 | 1.5 | 81.88 |
| B1 | 5 | 10.09 | 20.18 | 0.5 | 70.56 |
| B2 | 5 | 13.10 | 13.10 | 1.0 | 73.60 |
| B3 | 5 | 15.70 | 7.85 | 1.5 | 76.19 |
| C1 | 6 | 7.25 | 14.50 | 0.5 | 67.75 |
| C2 | 6 | 9.71 | 9.71 | 1.0 | 70.21 |
| C3 | 6 | 11.82 | 5.91 | 1.5 | 72.32 |

The air inlet of the guide vane is axial, and its airflow bending angle measures 40°. The C4 airfoil has been selected for this configuration. The guide vane blade in the back row contraction channel has been designed to be of the arc plate blade type. The outlet airflow angle is maintained at 40°; the design of the guide vane model was created using the 3D software Pro/E wildfire 5.0. A meridian view of the geometric model for each IGV is shown in Figure 4.

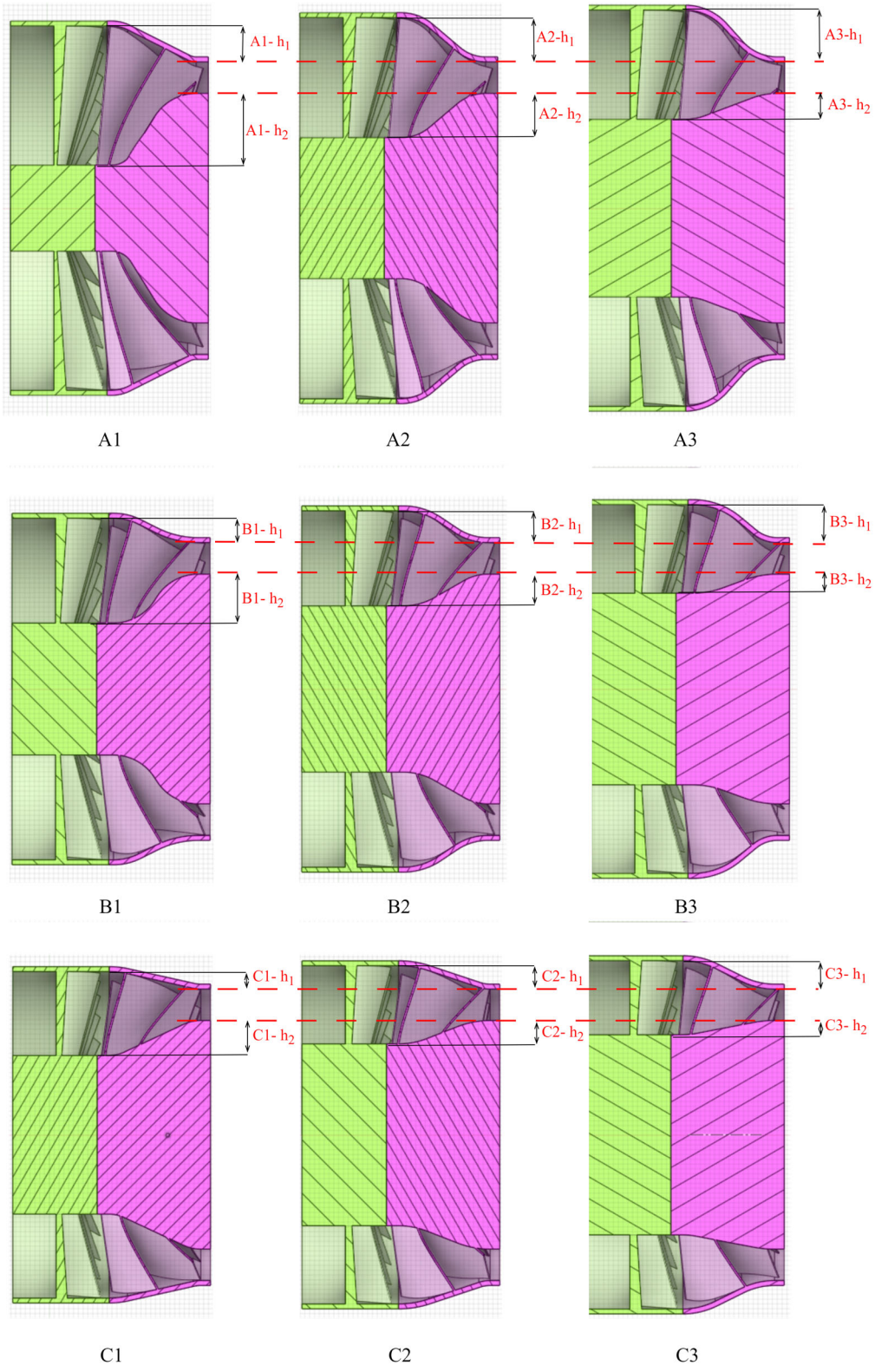



**Figure 4.** Meridian view of the geometric model for each IGV.

## 3. Numerical Simulation and Performance Testing

### *3.1. Computational Domain and Mesh*

The overall process of aerodynamic simulation is presented in Figure 5.

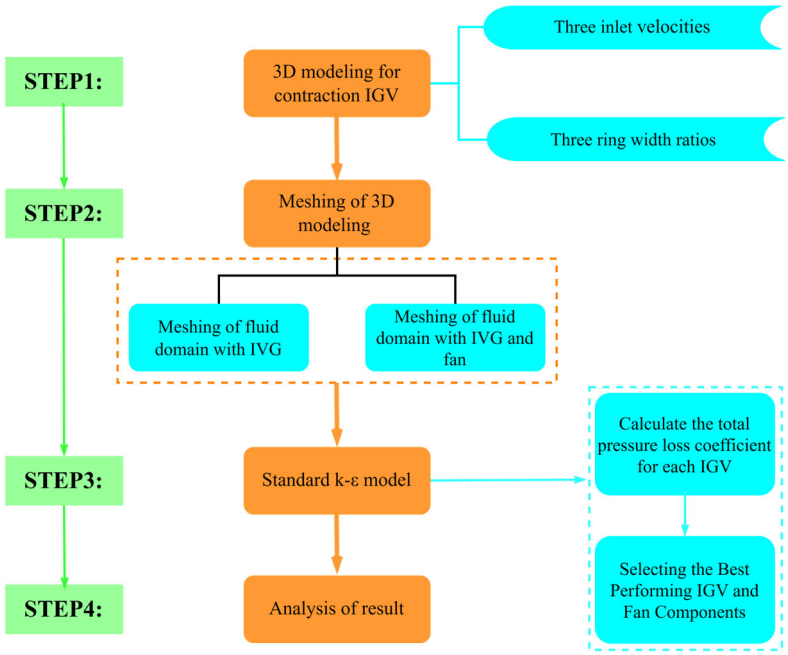
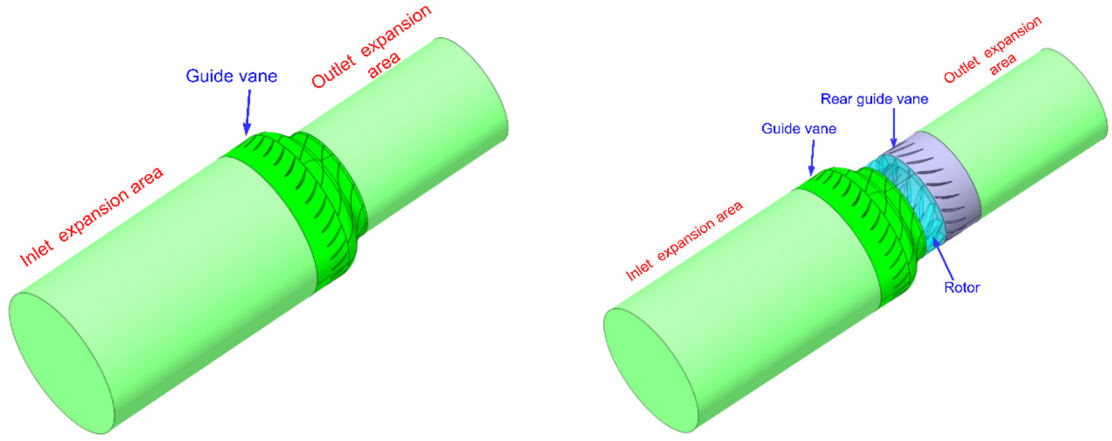



**Figure 5.** Overall process of the aerodynamic simulation.

ICEM CFD 2020 R2 software is used to generate the mesh grid for the IGV fluid domain with IGV structure and then complete the fan structure fluid domain combined with IGV and fan, as shown in Figure 6. In order to ensure the reliability of the numerical simulation, the inlet and outlet of the guide vane channel are extended, and the length of the inlet and outlet extension is 2.5 times the diameter of IGV. The guide vane computational domain is divided into inlet and outlet expansion area, pre-swirl guide vane area, and fan blade area; all the computational domain of the mesh is divided into structured grids. Figure 6 shows a schematic diagram of the computational domain.




(**a**) Single contraction IGV Fluid domain structure (**b**) Complete fan structure Fluid domain structure

**Figure 6.** Fluid domain structure.

### *3.2. Computational Models and Boundary Conditions*

The fluid flow of an IGV structure and the flow of a complete fan structure are numerically simulated respectively. The FLUENT 2023 R2 software is used to numerically calculate the fluid domain, the turbulence model is selected as the Standard k-ε model [28], and the pressure–velocity coupling is adopted by SIMPLE algorithm; the momentum equation, the energy equation, and the turbulence dissipation equation are solved using a second-order upwind scheme. No-slip boundary conditions are chosen for the computational wall, the

standard wall function is used in the near-wall area, the interfaces of each part are set to be interface interfaces, the inlet cross-section of the inlet expansion area is used as the entrance to the entire computational domain, the entrance boundary is set to be the velocity entrance, and the outlet is free outflow. The area of the rotor impeller is set as a rotating area, and the other areas are static areas. The interface between the regions uses interface boundaries to achieve a smooth transition of the fluid inside the turbine. The effects of gravity and wall roughness on the flow field are neglected in the calculation. When the residuals of each parameter are less than $10^{-4}$ and the total pressure of both inlet and outlet sections do not change with iteration time, the calculation is considered to have converged.

In order to ensure the accuracy of the calculation, the grid-independent validation of the single IGV calculation domain is conducted, as shown in Table 2. It has been observed that as the value of the grid number increases beyond 1.77 million, the calculated results tend to stabilize, so the grid number of 1.77 million is selected for the calculations. The total pressure loss coefficient at the outlet of the IGV is an important index for evaluating the reasonableness of the guide vane design, and the larger the total pressure loss coefficient, the worse the internal flow condition, which is defined as follows:

$$\varpi = \frac{P_{tot,in} - P_{tot,L}}{\frac{1}{2}\rho u_{out}^2} \tag{2}$$

where $P_{tot,in}$—total pressure at the inlet of the IGV, unit Pa; $P_{tot,L}$—local total pressure at the outlet of the IGV, unit Pa; $u_{out}$—average velocity at the outlet, unit m/s, $\rho$—air density, unit—kg/m$^3$.

**Table 2.** Grid independence study.

| Case No. | Number of Grid | Total Pressure Loss Coefficient $\varpi$ |
|---|---|---|
| 1 | $111 \times 10^4$ | 0.120 |
| 2 | $129 \times 10^4$ | 0.135 |
| 3 | $177 \times 10^4$ | 0.164 |
| 4 | $190 \times 10^4$ | 0.164 |
| 5 | $215 \times 10^4$ | 0.168 |

### *3.3. Performance Tests*

Sampling tests on the guide vane and pneumatic performance test were conducted using the AMCA2010 standard [29] test bench; the main equipment used in the test process includes an intelligent pressure transmitter, digital display instrumentation, and temperature and humidity sensors; the test bench structure is shown in Figure 7.

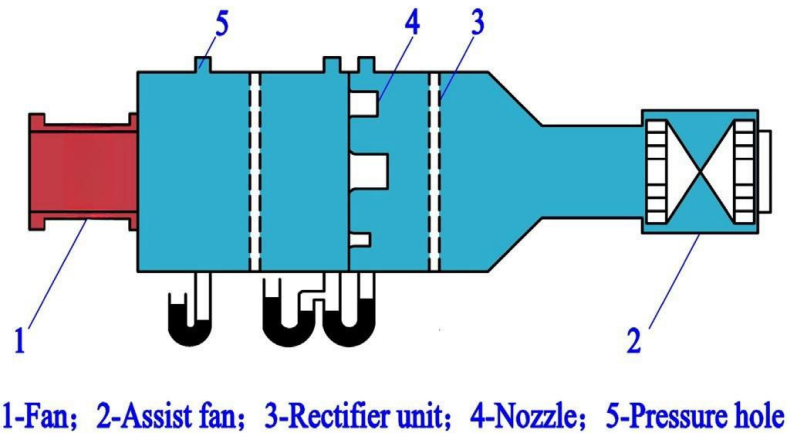



**Figure 7.** Test bench structure.

The physical drawing of the test bench is shown in Figure 8, during the test, the flow rate of the air chamber was varied by adjusting the speed of the auxiliary fan, while the inlet velocity of the IGV was also changed. The flow rate was determined by measuring the pressure difference before and after the nozzle, the total inlet pressure was set to atmospheric pressure, the value of the outlet static pressure was measured by an intelligent pressure transmitter, and the outlet dynamic pressure was calculated from the outlet flow rate. Table 3 shows the experimental environment data. The test bench is shown in Figure 8

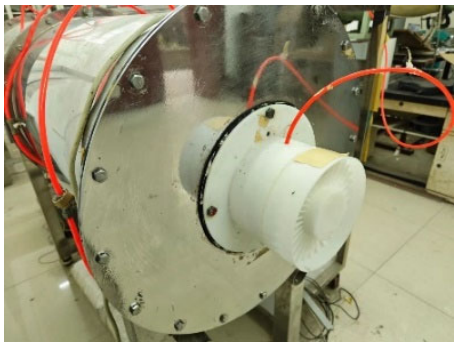


**Figure 8.** Physical drawing of the test bench.

**Table 3.** Experimental environment.

| Parameter | Value | Unit |
|---|---|---|
| Humidity | 52% | % |
| Temperature | 10.9 | °C |
| Pressure | 1028 | mbar |
| Density | 1.258 | $m^3/h$ |

### *3.4. Experimental Verification*

Figure 9 shows the total pressure loss coefficient curves of numerical simulation and experiment, respectively, and it can be seen that the trend of the performance curves obtained from simulation and experiment is basically the same, with a maximum error of 3.8%, which is within the permissible range of engineering.

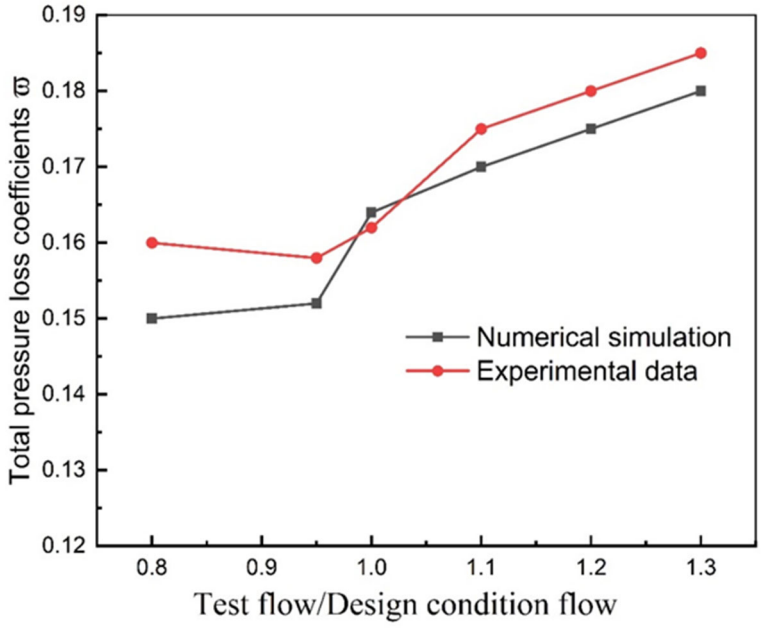



**Figure 9.** Comparison of simulated and experimental total pressure loss coefficients.

## 4. Results

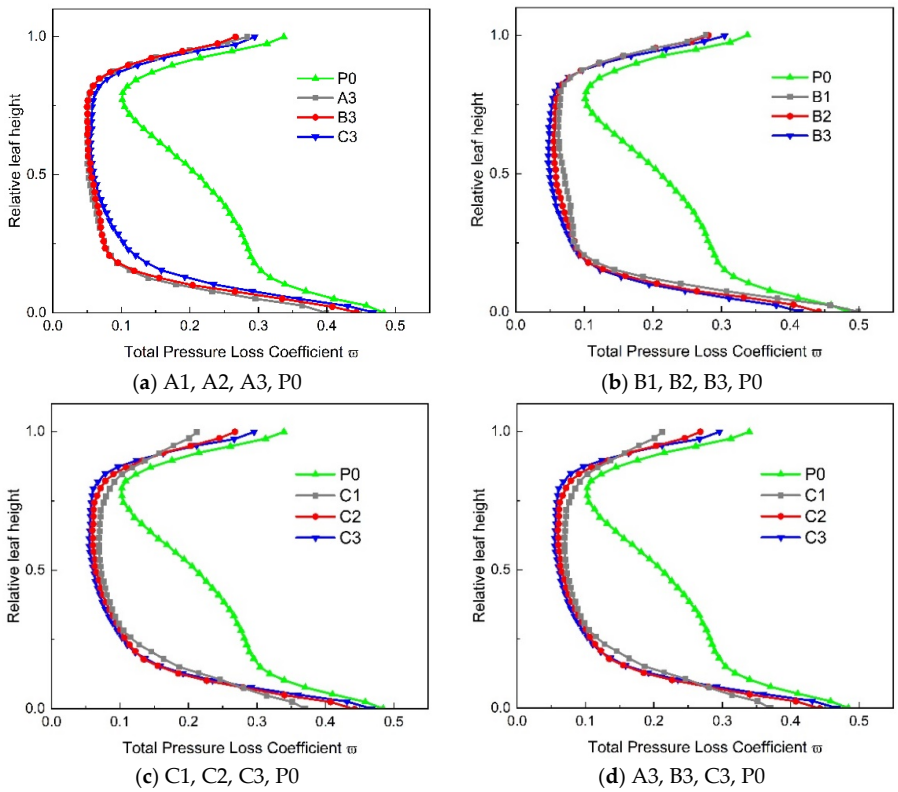
### *4.1. Performance Analysis of Inlet Guide Vane*

The total pressure loss coefficient of the IGV of each scheme is shown in Table 4.

**Table 4.** Total pressure loss coefficient.

| Case | Total Pressure Loss Coefficient $\varpi$ |
|---|---|
| P0 | 0.351 |
| A1 | 0.173 |
| A2 | 0.172 |
| A3 | 0.164 |
| B1 | 0.197 |
| B2 | 0.181 |
| B3 | 0.172 |
| C1 | 0.197 |
| C2 | 0.195 |
| C3 | 0.195 |

As illustrated in Figure 10, the distribution curve of the total pressure loss coefficient at the outlet of the guide vane for each scheme model and the prototype IGV along the blade height is presented. The total pressure loss coefficient at the outlet of the contraction IGV of the nine schemes is smaller than that of the prototype IGV in the entire blade height range. Among the leading vane schemes with the same inlet axial velocity, the schemes with the lowest total pressure loss coefficient are A3, B3, and C3; consequently, when the inlet axial velocity is constant, the greater the proportion of the outer annular surface width h1 of the second-stage vane channel, the higher the flow loss and total pressure loss of the guide vane.




(**a**) A1, A2, A3, P0 (**b**) B1, B2, B3, P0

(**c**) C1, C2, C3, P0 (**d**) A3, B3, C3, P0

**Figure 10.** Distribution of total pressure loss coefficients at the outlet of the guide vane along the spanwise for each IGV.

### *4.2. Fan Aerodynamic Performance Analysis*

#### 4.2.1. Performance Analysis

As illustrated in Figure 10d, the total pressure loss coefficient of the A3 scheme is the smallest, while the total pressure loss coefficient of the C3 scheme is the largest, when compared with the prototype. The contraction IGV of the A3 scheme (A3 IGV) was selected to be assembled with the rotor and rear guide vane (RGV) of the prototype fan. The fan parameters are shown in Table 5 [27].

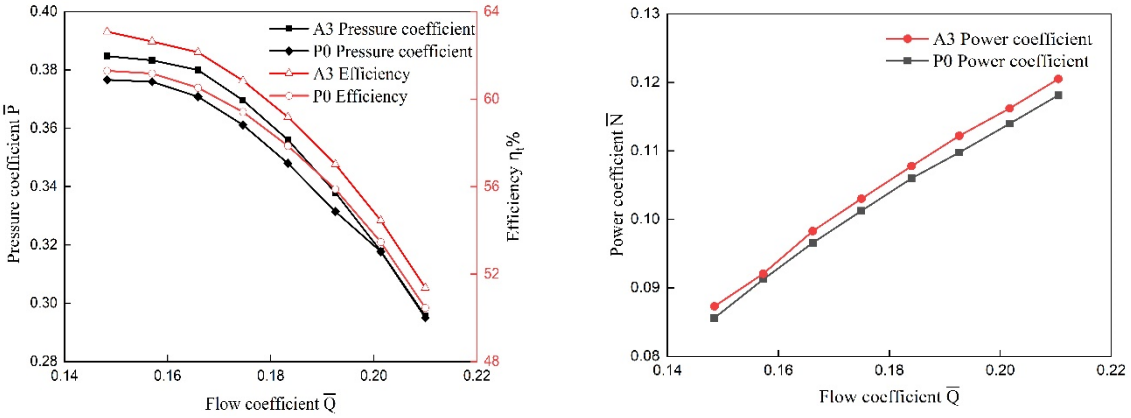
**Table 5.** Fan key design parameters.

| Design Parameter | Value | Unit |
|---|---|---|
| Design flow | 230 | $m^3/h$ |
| Desigen pressure | 600 | Pa |
| Rated speed | 5800 | rpm |
| Impeller diameter | 120 | mm |

The pressure coefficient $\overline{P}$, fan efficiency $\eta_t$, and power coefficient $\overline{N}$ are calculated by numerical simulation for 8 flow working points (flow conditions range from 0.95 design flow to −1.3 design flow), and Figure 11 shows the comparison curves of the external characteristics of the fan with A3 IGV and the fan with prototype guide vanes; in the design conditions, the pressure coefficient of the inlet guide vane fan of Scheme A3 is improved by 1.80% compared with that of the prototype fan. Under design conditions, the fan pressure coefficient of the solution with A3 IGV is improved by 1.80% compared to the prototype fan, and the fan efficiency is improved by 2.36%. Under small flow conditions, the near-stall point of the fan with Scheme A3 IGV is the same as that of the prototype fan, but the near-stall point fan efficiency is improved by 2.93% compared with that of the prototype fan; under large flow conditions, the pressure coefficients of the Scheme A3 fan and the prototype fan are almost equal. From Figure 11a, it can be observed that when the flow coefficient is between 0.147 and 0.186, the pressure coefficient curve of the Scheme A3 fan is above the pressure coefficient curve of the prototype fan, indicating that its working capacity is superior. When the flow coefficient is between 0.147 and 0.202, the efficiency curves of the fan with A3 IGV are consistently above those of the prototype fan, with an average efficiency improvement of 2.29% across the 8 flow conditions. From Figure 11b, it can be seen that the power consumption of the prototype fan is higher than that of the fan with A3 IGV in the range of flow conditions, which is consistent with the results of the fan—analysis. Especially in large flow conditions, the airflow in the channel flows uniformly with less separation, the flow field at the inlet of the moving blade is stable, and the power consumption of the whole fan is reduced. Therefore, the contraction IGV designed in this paper is of great significance to improve the internal flow condition of the fan, reduce the internal flow loss of the fan, and enhance the efficiency of the fan.

#### 4.2.2. Flow Analysis

Three flow conditions were selected for the structural analysis of the fan flow, with a flow coefficient of $\overline{Q}$ = 0.147 at the small flow condition point, a flow coefficient of $\overline{Q}$ = 0.155 at the design condition point, and a flow coefficient of $\overline{Q}$ = 0.186 at the high flow condition point.

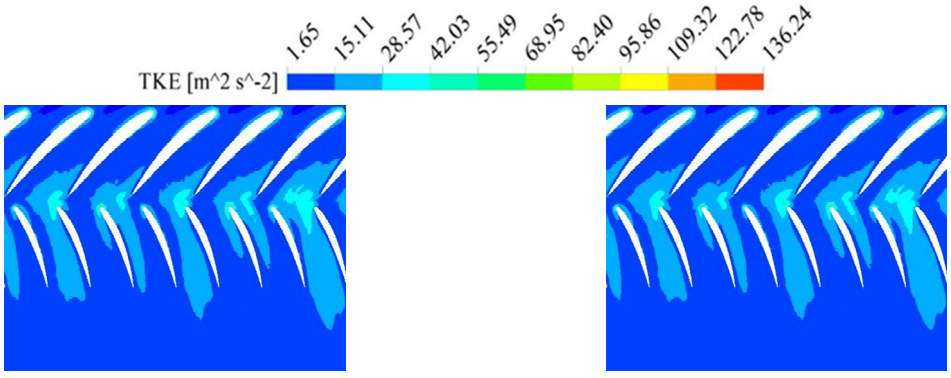



(**a**) $\bar{P} - \bar{Q}$ and $\eta_t - \bar{Q}$ (**b**) $\bar{N} - \bar{Q}$

**Figure 11.** Fan external characteristic curve.

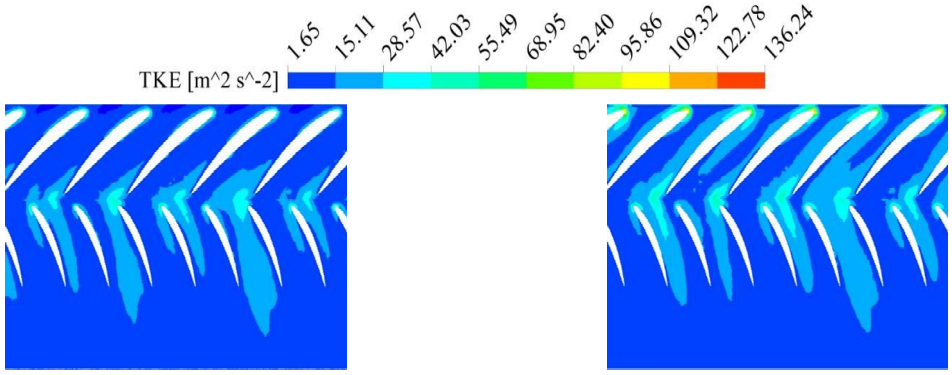
(1) Turbulent kinetic energy distribution

Figures 12–14 show the distribution of turbulent kinetic energy at 50% blade height of the rotor blade and RGV under small flow, design, and large flow conditions, respectively, and it can be seen by comparing the diagrams that, with the development of the fan condition from the small flow condition to the large flow condition, the area of the turbulent microgroups in the flow channel of the rotor and RGV gradually increases, leading to enhanced fluid pulsation and increased flow loss in the channels, which is one of the reasons for the decrease in the efficiency of fan with the increase in the flow rate. This is also one of the reasons why the fan efficiency decreases as the flow rate increases. Comparing the turbulent kinetic energy distribution of Scheme A3 and the prototype under three flow conditions, it can be seen that, on the one hand, the high turbulent kinetic energy region of the pressure side and the suction side of the rotor blade of Scheme A3 is significantly reduced compared with the prototype, especially near the stagnation point of the leading edge of the rotor blade, the vortex intensity is reduced, the flow condition of the rotor blade channel is obviously improved, and the boundary layer separation of the trailing edge of the rotor blade region is weakened. On the other hand, the airflow uniformity between the rotor blade and the RGV of the Scheme A3 fan is improved compared with the prototype flow uniformity, and the turbulent kinetic energy zone at 50% blade height is reduced. This shows that the contraction IGV has a great inhibitory effect on the development of turbulent flow in the rear stage of the fan. Therefore, the efficiency of the Scheme A3 fan is higher than that of the prototype fan under various flow conditions.



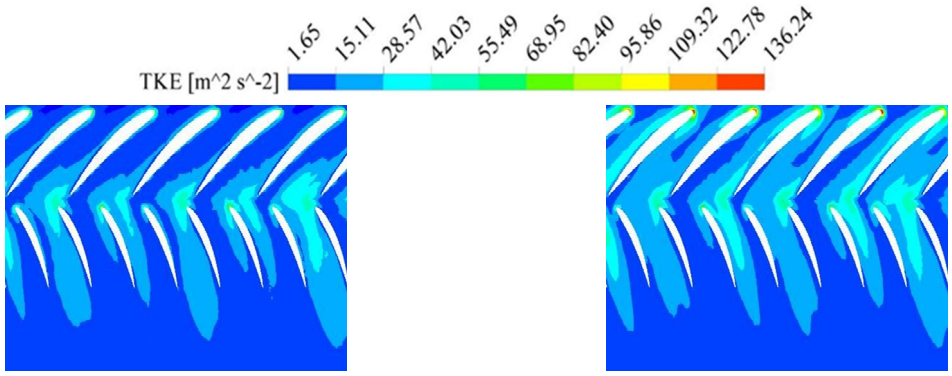

(**a**) A3 (**b**) P0

**Figure 12.** Turbulent kinetic energy distribution at 50% blade height of the moving vane and rear guide vane under low flow conditions.




(**a**) A3 (**b**) P0

**Figure 13.** Turbulent kinetic energy distribution at 50% blade height of the moving vane and rear guide vane under design conditions.

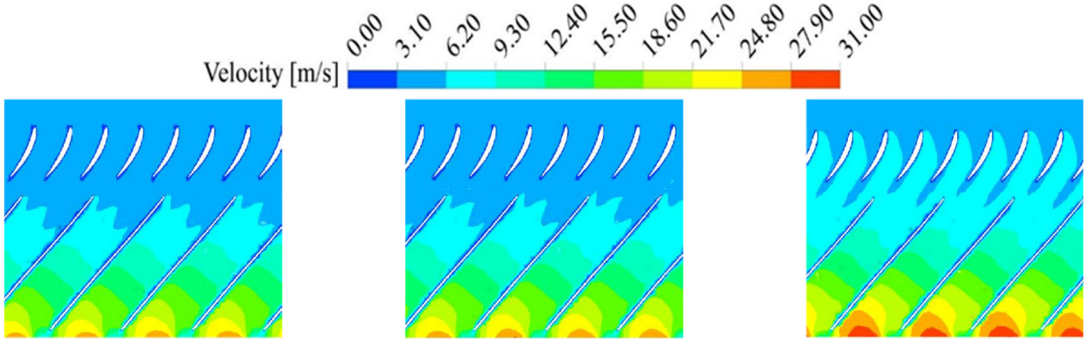



(**a**) A3 (**b**) P0

**Figure 14.** Turbulent kinetic energy distribution at 50% blade height of the moving vane and rear guide vane under high flow conditions.

(2) Velocity distribution

Figure 15 shows the distribution map of the IGV of Scheme A3 at 50% blade height under small flow conditions, design conditions, and large flow conditions. As the fan condition develops from a small flow condition to a large flow condition, the flow velocity of the IGV channel and outlet increases accordingly.



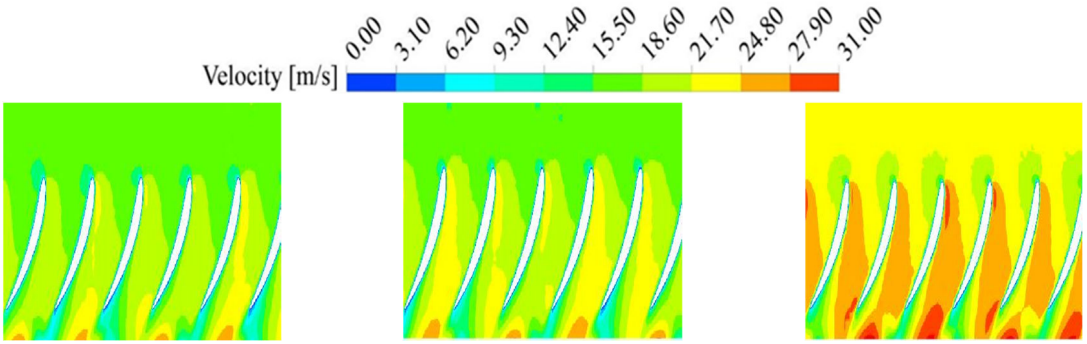

(**a**) A3 small flow (**b**) A3 design condition (**c**) A3 large flow

**Figure 15.** Velocity distribution at 50% blade height of A3.

Under the design condition, t the axial velocity of the airflow at the inlet of the pre-swirl guide vane for Scheme A3 is low, resulting in a small centrifugal force generated by the airflow during the turning process. Consequently, flow separation between the

pressure surface and the boundary layer of the suction surface of the blade is minimized, leading to uniform and relatively stable airflow in the first-stage guide vane channel. As illustrated in Figure 15b, after the airflow enters the rear guide vane, it is constrained by the contraction channel and the guide vane, which will make the gas maintain the original negative pre-swirl degree and accelerate in the channel. As the flow area gradually decreases along the axial direction, the airflow acceleration is more uniform, resulting in significantly reduced airflow separation and backflow on the blade surface.

The inner wall surface of the prototype IGV and the hub wall surface are cylindrical, with a small axial flow area. The flow area from the inlet to the outlet remains constant, and the velocity distribution at a height of 50% of the lobes of the prototype IGV is presented in Figure 16.




(**a**) P0 small flow (**b**) P0 design condition (**c**) P0 large flow

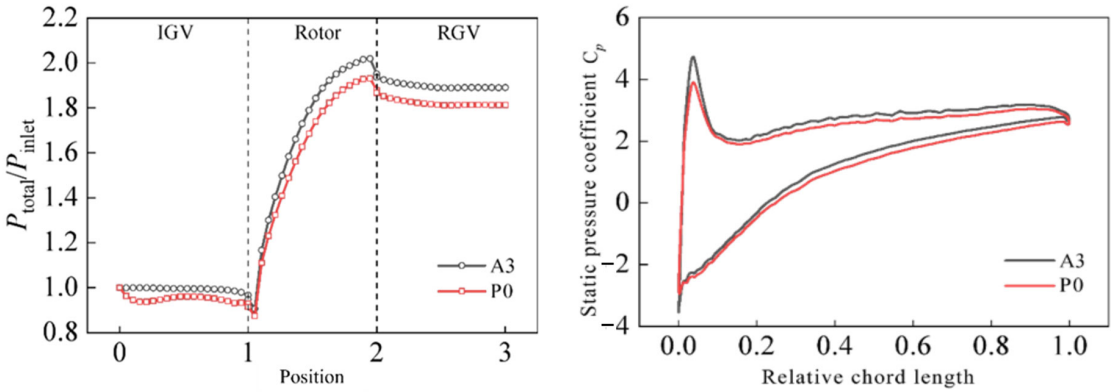
**Figure 16.** Velocity distribution at 50% blade height of the prototype.

As shown in Figure 16, as the airflow enters the prototype IGV during the folding process, the acceleration of the airflow is not uniform, resulting in the formation of a high-speed region near the suction surface of the blade. Additionally, a transverse velocity gradient is established from the suction surface to the pressure surface within the channel, causing the airflow near the trailing edge of the suction surface to separate from the surface layer and form a reflux region. This situation deteriorates flow conditions, leading to an increase in flow loss. Under small flow conditions, the velocity characteristics inside the IGV for Scheme A3, as shown in Figure 15a, are similar to those of the prototype IGV in Figure 16a and will not be further discussed. From Figures 15c and 16c, it can be observed that under high-flow conditions, a small low-velocity region forms at the leading edge of the prototype IGV. The transverse velocity gradient in the channel is more pronounced, with low-energy fluids accumulating at the trailing edge of the suction surface. Furthermore, airflow significantly separates from the flow at the trailing edge of the vane, leading to an expansion of the reflux zone. The effect of Scheme A3 on the uniform acceleration of airflow and stabilization of flow is particularly evident.

(3) Total pressure distribution along the flow direction and static pressure coefficient distribution

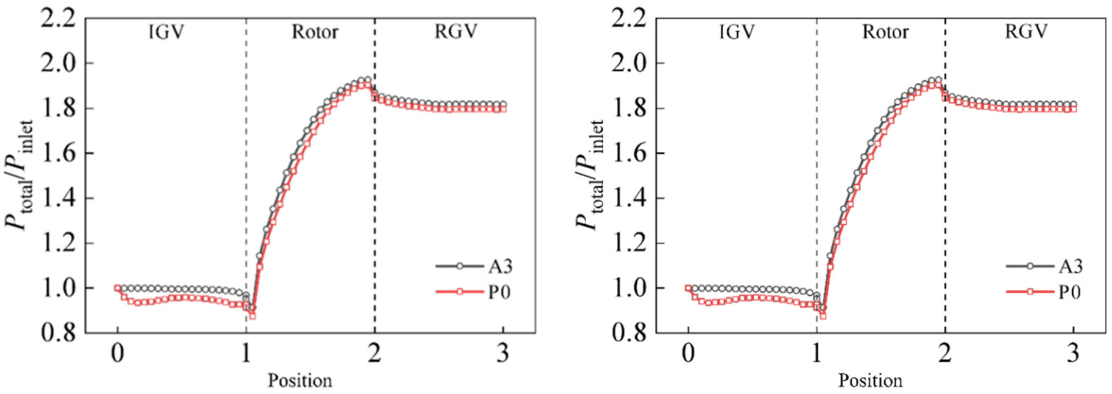
Figures 17–19 show the distribution curve of total pressure along the flow direction and the distribution of static pressure coefficient at 50% blade height of the entire fan under small flow conditions, design conditions, and large flow conditions, respectively. The fan of a small high-pressure axial flow machine is divided into three primary sections along the flow direction: IGV (0–1) in the IGV section, rotor (1–2) in the moving blade section, and RGV (2–3) in the rear guide vane section. The inlet and outlet extension sections are not analyzed. Among them, $P_{total}$ represents total pressure at the flow section position, and $P_{inlet}$ represents total pressure at the inlet section of the IGV. The total pressure at the flow

section position of each section is normalized. The $P_{total}/P_{inlet}$ values of the inlet of the IGV section of the Scheme A3 fan and the prototype are both 1.0.



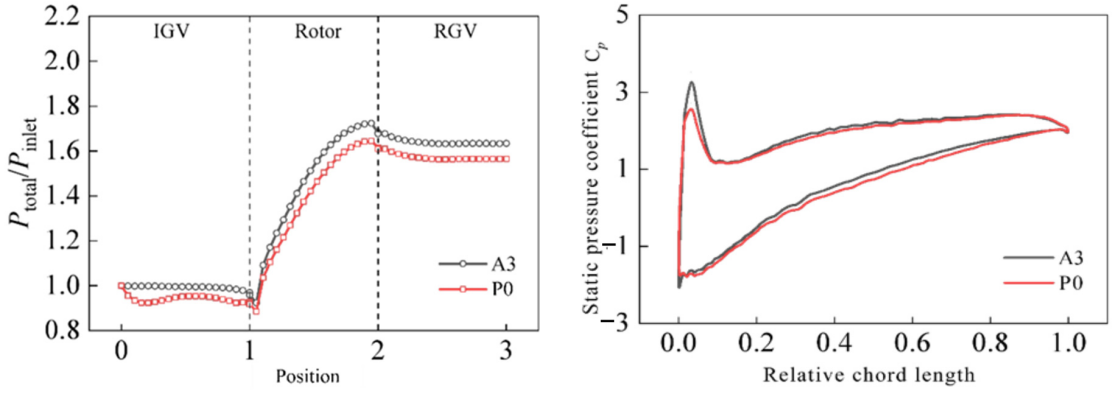

(**a1**) (**a2**)

**Figure 17.** Distribution of total pressure along the flow direction and distribution of static pressure coefficient under small flow conditions. (**a1**) The total pressure of the fan is distributed along the flow direction. (**a2**) The static pressure coefficient at 50% blade height of the rotor blade.




(**a1**) (**a2**)

**Figure 18.** Distribution of total pressure along the flow direction and distribution of static pressure coefficient under design conditions. (**a1**) The total pressure of the fan is distributed along the flow direction. (**a2**) The static pressure coefficient at 50% blade height of the rotor blade.




(**a1**) (**a2**)

**Figure 19.** Distribution of total pressure along the flow direction and distribution of static pressure coefficient for high flow condition. (**a1**) The total pressure of the fan is distributed along the flow direction. (**a2**) The static pressure coefficient at 50% blade height of the rotor blade.

As shown in Figures 17(a1), 18(a1) and 19(a1), as the fan conditions progress from small flow to large flow, the total pressure distribution curves for the Scheme A3 fan at the flow section positions (0–3) are consistently higher than those of the prototype fan, indicating that Scheme A3 of the IGV improves the working ability of the fan. In the IGV section, the total pressure drop of the Scheme A3 fan is significantly less than that of the prototype fan, indicating a smaller total pressure loss for the Scheme A3 IGV compared to the prototype under all flow conditions. In the moving blade section, the power capacity of the moving blade of the Scheme A3 fan is more obvious than that of the prototype moving blade under the small flow condition and the large flow condition. As the fan operating conditions transition to large flow conditions, the total pressure distribution trend for the moving blade sections of both schemes gradually flattens.

As shown in Figures 17(a2), 18(a2) and 19(a2), the blade load is the largest at the small flow condition point, and the blade load gradually decreases with the increase in the flow condition. The static pressure coefficient at 50% blade height of the fan rotor blade of Scheme A3 increases compared with the prototype under each flow condition, which is consistent with the distribution law of the total pressure of the fan rotor blade along the flow direction. Consequently, the IGV of Scheme A3 plays an important role in improving the fan's workability within the flow condition range.

## 5. Conclusions

This paper studies a variety of guide vane flow channel schemes featuring a tandem and contraction structure. The airflow turning angle reaches 40°. Numerical simulation analyses and experimental verifications of the IGV model for each scheme are performed and applied to a small high-pressure coefficient axial flow fan. The following conclusions are obtained:

(1) In this paper, the flow loss is effectively reduced by increasing the inlet area and using a contraction channel to accelerate the gas slowly. Increasing the ratio of outer ring height can effectively reduce the total pressure loss coefficient with the same inlet ring area. The optimal result is achieved when the ring width ratio is 1.5, leading to a 53.11% reduction in total pressure loss compared to the basic model, thereby minimizing flow loss.

(2) Utilizing the methods of a contraction channel and tandem blades effectively suppresses turbulence development in the fan flow field and more uniform velocity distribution of the gas in the guide vanes, reducing gas flow losses in the guide vanes, resulting in an average fan efficiency increase of 2.29% under all flow conditions. The total pressure curve is also higher than the prototype, and the effect is more obvious under large flow conditions.

(3) The pre-swirl structure of the t contraction guide vanes designed in this paper offers significant reference value for enhancing the theoretical energy and is well-suited for compact machine designs with stringent structural size constraints.

**Author Contributions:** Conceptualization, Q.S. and B.Q.; methodology, Q.S. and B.Q.; software, B.Q.; validation, Q.S., J.Z. and L.M.; formal analysis, B.Q.; investigation, B.Q.; resources, Q.S.; data curation, B.Q.; writing—original draft preparation, B.Q.; writing—review and editing, Q.S.; visualization, B.Q. and L.M.; supervision, Q.S.; All authors have read and agreed to the published version of the manuscript.

**Funding:** This research received no external funding.

**Data Availability Statement:** The data presented in this study are available on request from the corresponding author due to the research content of the topic is not yet finished, and subsequent studies will need to use the data in this paper.

**Conflicts of Interest:** The authors declare no conflict of interest.

## References


1. Liu, M.; Tan, L.; Cao, S. A review of pre-whirl regulation by inlet guide vanes for compressor and pump. *Proc. Inst. Mech. Eng. Part A J. Power Energy* **2018**, *233*, 803–817. [CrossRef]
2. Danlos, A.; Podevin, P.; Toussaint, M. Pre-swirl mechanism in front of a centrifugal compressor: Effects on surge line and on unsteady phenomena in surge area. *MATEC Web Conf.* **2017**, *133*, 04002. [CrossRef]
3. Zheng, X.; Huang, Q.; Liu, A. Loss Mechanisms and Flow Control for Improved Efficiency of a Centrifugal Compressor at High Inlet Prewhirl. *J. Turbomach.* **2016**, *138*, 101011. [CrossRef]
4. Sonoda, T. Experimental Investigation on Spatial Development of Streamwise Vortices in a Turbine Inlet Guide Vane Cascade. *Int. J. Turbo Jet Engines* **1987**, *4*, 85–96. [CrossRef]
5. Fukutomi, J.; Nakamura, R. Performance and Internal Flow of Cross-Flow Fan with Inlet Guide Vane. *JSME Int. J.* **2005**, *48*, 763–769. [CrossRef]
6. Liu, H.J.; Ouyang, H.; Tian, J.; Li, Y. Aerodynamic and Aeroacoustic Study on the Cross Flow Fan with Inlet Guide Vane. *Kung Cheng Je Wu Li Hsueh Pao/J. Eng. Thermophys.* **2012**, *33*, 236–239.
7. Goto, A.; Zangeneh, M. Hydrodynamic design of pump diffuser using inverse design method and CFD. *J. Fluids Eng.* **2002**, *124*, 319–328. [CrossRef]
8. Kim, J.H.; Ahn, H.J.; Kim, K.Y. High-efficiency design of a mixed-flow pump. *Sci. China Technol. Sci.* **2010**, *53*, 24–27. [CrossRef]
9. Kim, J.H.; Kim, K.Y. Optimization of Vane Diffuser in a Mixed-Flow Pump for High Efficiency Design. *Int. J. Fluid Mach. Syst.* **2011**, *4*, 172–178. [CrossRef]
10. Oro, J.M.F.; Díaz, K.M.; Morros, C.S.; Marigorta, E.B. On the structure of turbulence in a low-speed axial fan with inlet guide vanes. *Exp. Therm. Fluid Sci.* **2008**, *32*, 316–331.
11. Del Greco, A.S.; Tapinassi, L. On the combined effect on operating range of adjustable IGVS and variable speed in process multistage centrifugal compressors. In Proceedings of the ASME Turbo Expo 2013: Turbine Technical Conference and Exposition, San Antonio, TX, USA, 3–7 June 2013; Oil and gas applications; Steam turbines: ASME (American Society of Mechanical Engineers) turbo expo: Turbine technical conference and exposition; ASME: Houston, TX, USA, 2013; Volume 5B.
12. Coppinger, M. Aerodynamic Performance of an Industrial Centrifugal Compressor Variable Inlet Guide Vane System. Ph.D. Thesis, Loughborough University, Loughborough, UK, 1999.
13. Song, Z.; Li, X.; Liu, Z. Study on the mechanism of the influence of inlet precession on the aerodynamic performance of centrifugal impellers. *J. Appl. Mech.* **2021**, *38*, 53–59.
14. Huang, L.; Liu, Y.; Chen, H. Inlet Swirl on Turbocharger Compressor Performance. In Proceedings of the 16th International Symposium on Transport Phenomena and Dynamics of Rotating Machinery: ISROMAC 2016, Honolulu, HI, USA, 10–15 April 2016.
15. Wang, Y.C.; Shi, M.; Cao, S.L.; Li, Z.H. Numerical investigation on pressure fluctuations in centrifugal compressor with different inlet guide vanes pre-whirl angles. *IOP Conf. Ser. Mater. Sci. Eng.* **2013**, *52*, 042001. [CrossRef]
16. Zhao, J.; Wang, Z.; Xi, G.; Zhang, X.; Lan, A.; Gong, W. Investigation of Performance and Flow Field of a Centrifugal Compressor Under Negative Pre-Swirl. *Turbo Expo Power Land Sea Air* **2015**, *56659*, V02CT42A026.
17. Liu, M.; Tan, L.; Cao, S.L. Influence of prewhirl angle on a centrifugal pump with inlet guide vane running at turbine mode. *IOP Conf. Ser. Earth Environ. Sci.* **2019**, *240*, 032013. [CrossRef]
18. Okiishi, T.H.; Junkhan, G.H.; Serovy, G.K. Experimental Performance in Annular Cascade of Variable Trailing-Edge Flap, Axial-Flow Compressor Inlet Guide Vanes. In Proceedings of the ASME 1970 International Gas Turbine Conference and Products Show, Brussels, Belgium, 24–28 May 1970.
19. Liu, M.; Jiang, Y.M.; Chen, T. Influence of the blade-guide vane clearance on the unsteady performance of a mixed-flow pump. *Chin. J. Hydrodyn.* **2019**. Available online: https://xueshu.baidu.com/usercenter/paper/show?paperid=1u3u0m600y4x04m0r85406u0u2562230&site=xueshu_se (accessed on 16 February 2025).
20. Najjar, Y.S.H.; Akeel, S.A.M.S. Effect of Prewhirl on the Performance of Centrifugal Compressors. *Int. J. Rotating Mach.* **2007**, *8*, 397–401. [CrossRef]
21. Zhang, Y.; Qi, D.; Mao, Y. Experimental investigation and improvement of the inlet guide vane with plate vane in a centrifugal fan. *Proc. Inst. Mech. Eng. Part A-J. Power Energy* **2009**, *223*, 401–413. [CrossRef]
22. Crouse, J.E.; Steinke, R.J. *Preliminary Analysis of the Effectiveness of Variable-Geometry Guide Vanes to Control Rotor-Inlet Flow Conditions*; National Aeronautics ANDI SPACi Administration: Washington, DC, USA, 1967.
23. Dong, Y.; Zhao, Q. Experimental Research on Performance Optimization of Fans with Variable Curvature Static Guide Vanes. *Aviation Engines* **1996**, *3*, 27–29+15. Available online: https://kns.cnki.net/kcms2/article/abstract?v=tOz5m-jLbAWb9n1bqipzvu1tOxrXFHSsjE3naGyCbRwXQLG9biwNU9HRL6IeRmsx0w6j0JhTf90v080j7FB8kywmhlQvdkgSroq0eKcgMkNISJvec-BEShfFpst6jciVQEabPgabD0hI2kAVXlAdlk6aMSY2MPf_&uniplatform=NZKPT (accessed on 16 February 2025).
24. Smith, L.H., Jr. NASA/GE Fan and Compressor Research Accomplishments. *Am. Soc. Mech. Eng.* **1994**, *116*, 555–569.

25. Reed, V.L.; Schneider, P.W. Part-Span Variable Inlet Guide Vanes for V/STOL Fan Thrust Modulation. *J. Aircr.* **2015**, *19*, 52–57. [CrossRef]
26. Boehle, M.; Cagna, M.; Itter, L. Compressible Flow in Inlet Guide Vanes with Mechanical Flaps. *ASME Turbo Expo Power Land Sea Air* **2004**, *41707*, 341–349.
27. Xiao, G.; Sai, Q.; Liu, Y. Study on the effect of accelerated IGV on the performance of highly loaded axial fans. *J. Chongqing Technol. Bus. Univ. (Nat. Sci. Ed.)* **2024**, *41*, 42–49.
28. Ye, X.; Li, P.; Li, C. Study on performance and vibration characteristics of axial fan with double groove tip structure. *J. Mech. Eng.* **2015**, *51*, 167–174. [CrossRef]
29. *AMCA 210-07*; Standard for Testing Air Performance of Fans. Air Movement and Control Association International, Inc.: Arlington Heights, IL, USA, 2010.

**Disclaimer/Publisher's Note:** The statements, opinions and data contained in all publications are solely those of the individual author(s) and contributor(s) and not of MDPI and/or the editor(s). MDPI and/or the editor(s) disclaim responsibility for any injury to people or property resulting from any ideas, methods, instructions or products referred to in the content.